



UNIVERSITÀ
DEGLI STUDI
DI UDINE

Università degli studi di Udine

Multiscale simulation analysis of passive and active micro/nanoelectrodes for CMOS-based in vitro neural sensing devices

Original

Availability:

This version is available <http://hdl.handle.net/11390/1227337> since 2022-06-13T23:01:20Z

Publisher:

Published

DOI:10.1098/rsta.2021.0013

Terms of use:

The institutional repository of the University of Udine (<http://air.uniud.it>) is provided by ARIC services. The aim is to enable open access to all the world.

Publisher copyright

(Article begins on next page)

PHILOSOPHICAL
TRANSACTIONS A

rsta.royalsocietypublishing.org

Research



Article submitted to journal

Subject Areas:

Bio-electronics, Modelling and
Simulation, Neuron activity sensors

Keywords:

Neuronal Recordings, TCAD,
Modelling, Bio-interfaces,
Hodgkin-Huxley model

Author for correspondence:

Federico Leva

e-mail: federico.leva@unimore.it

THE ROYAL SOCIETY
PUBLISHING

Multiscale simulation analysis of passive and active micro/nano-electrodes for CMOS-based *in-vitro* neural sensing devices

Federico Leva¹, Pierpaolo Palestri² and
Luca Selmi¹

¹ Dipartimento di ingegneria Enzo Ferrari, University of
Modena and Reggio Emilia, Modena, Italy.

² Polytechnical Department of Engineering and
Architecture, University of Udine, Udine, Italy.

Neuron and neural network studies are remarkably fostered by novel stimulation and recording systems, which often make use of biochips fabricated with advanced electronic technologies and, notably, micro- and nanoscale CMOS. Models of the transduction mechanisms involved in the sensor and recording of the neuron activity are useful to optimize the sensing device architecture and its coupling to the readout circuits, as well as to interpret the measured data.

Starting with an overview of recently published integrated active and passive micro/nano-electrode sensing devices for *in-vitro* studies fabricated with modern (CMOS based) micro-nano technology, this paper presents a mixed-mode device-circuit numerical-analytical multiscale and multiphysics simulation methodology to describe the neuron-sensor coupling, suitable to derive useful design guidelines. A few representative structures and coupling conditions are analyzed in more detail in terms of the most relevant electrical figures of merit including signal-to-noise ratio.

1. Introduction

In recent years powerful alternatives to the well established patch clamps have emerged in the form of passive or active microelectrodes respectively connected to recording instrumentation or to custom integrated circuits. These electrodes can match the size of individual biological entities at the cellular, subcellular or even

© The Authors. Published by the Royal Society under the terms of the Creative Commons Attribution License <http://creativecommons.org/licenses/by/4.0/>, which permits unrestricted use, provided the original author and source are credited.

molecular level [1–4], yielding new solutions for neuron sensing (and stimulation).

Furthermore, they can be conveniently realized, in passive or active pixel form, as densely packed arrays suited to monitor individual neurons and networks. Well established complementary metal-oxide semiconductor (CMOS) technology, offers the opportunity to locally multiplex and condition the signals on-chip, thus avoiding the interference and attenuation induced by long interconnects [1,5–7]. Moreover, by adapting the back-end-of-line (BEOL) process technology, the electrode stability and the biocompatibility in physiological environments can be improved [1,2,7]. As a result, a neuron culture can be placed or grown onto the array, and the chip can then simultaneously perform individual subcellular investigations of several neurons while mapping an entire neural network [7]. For all these reasons, semiconductor technology-based neural recording systems constitute today the backbone of many *in-vitro* [8–10] (and *in-vivo* [9–11]) neural activity sensors, although deformable sensor devices and those directly integrated by means of electronic-mechanical assemblies with biological systems can be found as well [12–14].

Understanding how to achieve high-fidelity, high spatio-temporal resolution and reliable neuron-to-chip coupling for sensing is of paramount importance in view of many applications [8, 15,16]. Also, revealing the multiple signal paths that eventually lead to the waveform generation is also important to enable more accurate spike identification, sorting, fingerprinting, etc.

In this respect, modeling, simulation, and electronic design automation (EDA) tools play a key role. However, they are not so developed for describing the electronics/electrolyte/neuron coupling. At present, models of this coupling are almost exclusively defined as equivalent circuits [17–19], and the unknown model parameters are estimated *ex-post* by fitting measured data [20], or by examining the cell/sensor adhesion by means of few TEM/SEM images that kill the cell cultures [21,22]. Modelling the physics and geometry of the bio-electronic interface with suitable CAD tools, instead offers the opportunity to consider more realistic 3D geometries and the complex physical phenomena involved [23]. Physical simulations can also support the definition, validation and calibration of equivalent circuit. Lastly, physics-based CAD accommodates descriptions of the physical, biological and electronic subdomains, enabling the simultaneous optimization of the whole system.

In this paper, after a short overview of recent electronic sensor architectures for *in-vitro* neural recording useful to motivate the following research, we describe an approach to model the neuron/sensor interface and readout electronics on the same physics-based simulation platform with a mixed-mode finite element/circuit approach. The new simulation framework bridges the gap between hardware and wetware, enables the simultaneous optimization of the sensor device and the readout, while taking into account the neuron environment.

The paper is structured as follows: Section 2 overviews the technological background of the sensing systems and compares the performances of a few selected solutions. Section 3 details our proposed methodology, combining lumped elements' equivalent circuits and finite element numerical models (FEM). Section 4 reports representative analysis of a few case studies in terms of transient response to action potentials (APs), neuron-to-readout transfer functions, and signal-to-noise ratio (SNR) estimation. Finally, conclusions are given in Section 5.

2. Background

In the following subsections we overview a few recently published neural sensing devices that exploit micro-nanoelectronic fabrication, possibly integrated in a CMOS backbone. Their salient features define the general architecture of a few template structures (shown in Fig. 1) which are then considered for detailed analysis in Section 4.

(a) Overview of extracellular recording devices

Passive (i.e., without on-site amplification) micro-electrode arrays (MEAs) have been the workhorse for extracellular signal electrophysiology [24,25]. They mostly consist of arrays of

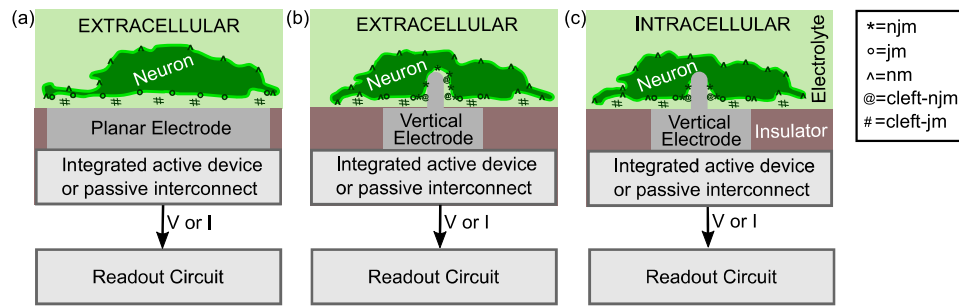


Figure 1. Schematic cross sectional representation of a few template devices for neuron sensing: planar electrode (a), and planar electrode with vertical needle protrusion (b and c). The needle couples to the neuron via a thin cleft (extracellular coupling, b) or penetrates the cell membrane (intracellular coupling, c). The membrane is partitioned in the nano-junctional, (njm), junctional, (jm), and non-junctional, (nm), compartments. The nano-junctional and junctional electrolytic clefts between the membrane and the electrodes are also shown, according to the notation introduced in [19].

planar electrodes (Fig. 1.a) with $5 \div 30 \mu\text{m}$ diameter [8]. MEAs record large scale extracellular field potentials (FPs) for days and months without damaging the cells. However, neurons typically do not stand closer than 70–100 nm to planar electrodes [26]. Consequently, the sensor weakly couples to the neural signals and the sensed FP amplitudes are extremely small ($10 \div 100 \mu\text{V}$). Moreover, the FPs reflect the attenuated, spatio-temporally filtered and overlapped action potentials (APs), synaptic potentials, and slow glia potentials, of a large number of excitable cells [27]. As a result, subcellular (e.g., ionic channel current) and subthreshold information are difficult to detect, and intensive data post-processing is deployed to extract and sort out the recorded signals [27].

Limitations of passive MEAs can be partly overcome by acting on the signal transduction chain and/or on the microelectrode morphology and coating. For instance, by connecting them to a field-effect transistor, FET [28], it is possible to amplify the signals *in-situ*, thus driving more effectively the wiring capacitance and resistance and eventually increasing the recorded signal [27] (see also Section 4). Fromherz's pioneering work successfully demonstrated planar electrodes integrated on top of an FET where the electrolyte surrounding the neurons acts as a gate that modulates the channel conductance [28–31] driven by the neurons' spikes. The integration of electrodes in the BEOL of CMOS chips delivers parallel recording platforms, as represented by the CMOS-MEA5000 market solution [32], with its 4225 recording sites, and beyond (65536) in a research demonstration [33] (#2 in Tab. 2).

Another way to improve the signal quality is to fabricate on top of planar electrodes small and tall vertical protrusions which create fine scale neural interfaces (Fig. 1.b) where specific local interactions occur [34]. The nano-electrodes enable interrogations of the neuron largely decoupled from the background signals of the surrounding cells. A good lateral sealing with a reduced cleft thickness of less than 5 nm [21] also beneficially affects sensitivity by short circuiting the electrical double layers (EDLs) at the cleft's interfaces. Local and tight contact with the neuron membrane has been demonstrated, e.g., with mushroom-shaped protrusions [27,35–37], or with nanoneedles/nanowires [27,38,39].

Mushrooms-shaped microelectrodes are engulfed by the cells through an endocytotic-like process [27] facilitated by the mushroom cap's curvature [36], especially if the diameter does not exceed 2–2.5 μm [35] (#1 in Tab. 2). To increase mushrooms' coupling to neurons up to 100-fold, a conductive polymer coating (e.g., PEDOT:PSS) can be used [37] (#7 in Tab. 2). A capacitance increase from 5 to 500 $\mu\text{F}/\text{cm}^2$ has been observed [40] compared to the double-layer capacitance onto bare gold electrodes [41]. Experimental evidences suggest that also high aspect-ratio vertical nanowires with diameter around 200 nm are engulfed by neurons without internalization [38].

A disadvantage of the protrusion is the reduced contact area, that implies higher electrode impedance, reduced coupling and increased noise. Mini-arrays of few 3D vertical nano-protrusions on the same electrode allow to recover the low electrode impedance [10]. Also the reliability, the amplitude of recordings and the SNR are improved compared to planar MEAs [8] with one or no vertical protrusions. An alternative solution aims to improve sealing by reverting the protrusions into a hollow in the microelectrode [39].

In all these cases the optimal protrusion/hollow morphology is still unknown and the ability to predict the electrode impedance ahead of fabrication would support performance optimization. Furthermore, the integration of protrusions with an amplification unit per sense/stimulation site results in extracellular sensing platforms with unprecedented recording quality, as both the coupling and the sealing are maximised. A notable example is the active 3D-shaped CMOS nano-electrode array (CNEA) platform in [39,42] (#6 in Tab. 2).

Extracellular sensors are nevertheless inherently limited by a low signal, introduce distortions of the recorded AP waveform, and do not carry the whole spectrum of information as their intracellular counterparts (Fig. 1.c). In fact, the extracellular recorded signal also depends on the neuron-electrode adherence and on the aggregation of ion channels at the interface [17,18]. To overcome these limitations significant work has been devoted to intracellular sensors, also based on semiconductor device fabrication processes, as discussed in the following Section.

(b) Overview of intracellular recording devices

The sensor size and geometry are crucial to attain stable access the intracellular medium; both should be optimized for the purpose. Sharp protruding vertical nanowires/nanoneedles with diameter ≤ 100 nm can promote spontaneous cell penetration as the result of cell-sensor adhesion-mediated forces and active cellular processes such as endocytosis [43], see for instance the high aspect-ratio vertical nanoneedles' array in [44] (#4 in Tab. 2). However, such a miniaturized sensor suffers of small coupling capacitance essentially because of the reduced contact area. Passive sensors become unfeasible with such tiny devices. Therefore, active sensing architectures are preferred for deep sub-micron spatial resolution, as will be discussed in Sections 3 and 4.

Spontaneous penetration alone does not ensure reliable intracellular access. Penetration can be improved via centrifugation forces to push the cell onto the nanoneedles [43], or chemical surface modification with adhesion molecules [45]. However, non-spontaneous penetration damages the membrane and leads to cell death, significantly reducing the duration of the recordings [8].

Alternatively, random-shaped miniaturized pores can be created in the lipid membrane by voltage or current injection. This so called *electroporation* releases the constraints on the sensor shape, because the nano-electrode does not need to pierce the membrane. However, it perturbs the spontaneous cell activity [38] and causes blind recording periods [8]. Furthermore, electroporation activates repair mechanisms that re-seal the nanopores [46]; only repeated electrical pulses can maintain the poration needed to realize long-term recordings [8]. Along this line of thought, a novel, continued current-injection electroporation method has been proposed for the CNEA platform (#6 in Tab. 2), delivering up to 19 minutes of intracellular signal recordings [39].

As an alternative, *optoporation* at the tip of gold nanoneedles, excited by short laser pulses, locally and precisely generates individual pores down to one nanometer size [38] (#3 in Tab. 2). Optoporation obviates to the blind recording periods of electroporating electrodes. By shining a single laser pulse onto an array of gold nanoneedles, a continuous intracellular recording up to 80 minutes has been demonstrated [38].

Lastly, electrode *biochemical functionalization* has been proposed [43,47], which reduces the leakage of the cytoplasm toward the extracellular electrolyte, and improves intracellular access repeatability, thus enabling long-term recordings [8]. Recently, Lieber *et al.* extended previous works on cultured cardiomyocyte cells [49–51], demonstrating arrays of 168 individually addressable U-shaped nanowire FET probes for neural intracellular sensing [48] (#5 in Tab. 2). The U-FET brings the gated channel of a FET in intimate contact with the intracellular

fluid, thus implementing active intracellular sensing. Voltage amplitudes comparable to those of patch-clamps have been recorded [48].

Despite these remarkable successes, however, achieving a stable and durable contact with the intracellular fluid, repeatable over time with the same culture, remains a persistent challenge [39].

(c) Specifications and benchmark of sensing solutions

For the purpose of setting the nomenclature, Fig. 1 sketches a few microelectronic neuron sensing devices with some of the salient features encountered in the previous overview. The neuron interacts either with planar electrodes (a) or with a protruding vertical electrode (b and c). Any of these electrodes can be locally connected to an integrated active device (e.g., a FET) or to a passive interconnect that propagates the electrical signal to the readout circuit.

Ideally, these neural sensing devices should be capable to monitor, with sampling times in the sub-ms range, the dynamics of the transmembrane voltage including both excitatory and inhibitory subthreshold synaptic potentials (e.g., non firing AP), as well as membrane oscillations [27,52], as summarized in Tab. 1. Merging the requirements therein, an approximate 0.1 Hz-10 kHz measurement bandwidth is needed to embrace with some margin all the above mentioned signals [39].

	Membrane Oscillation	Excitatory and Inhibitory Subthreshold Potential	Intracellular Action Potential
Amplitude [mV]	± 5	$\pm 0.5 \div 10$	$-80 \div 30$
Duration [ms]	n.a.	$<1(\text{rise})/100\text{-}1000(\text{decay})$	$1\text{-}2 + \text{*AHP}$
Spectrum [Hz]	1-50	100	500-1000

Table 1. Requirements for neural sensing devices adequate to capture the entire neurons' bio-signalling repertoire. *AHP= after-hyperpolarization phase which can be *fast* (2-5 ms), *medium* (5-100 ms), or *slow* (1-2 s) [52]

Since performance benchmarks in literature mostly focus on materials and fabrication processes [10,19,27], we compare in Tab. 2 in terms of electrical figures of merit a selection of literature results referenced in the previous section and, among these, estimates of the sometimes neglected but nevertheless important signal-to-noise ratio, SNR. We should stress that the aim of this comparison is not to spot the best system, but rather to discuss the main trends related to the combinations discussed previously, i.e., active or passive sensor combined with intra- or extracellular access.

We see that the largest signal amplitudes are measured when intracellular access is established via spontaneous incorporation or electrical and optical poration methods. A large signal amplitude does not always come with high SNR, though. In fact, the SNR depends on many system features, including those of the readout circuit. Active pixels are less sensitive to the interconnect parasitics, making it easier to implement parallelization and to operate a large number of recording sites. We also see that extracellular access allows for days/months recordings, although the measured signal amplitude is much lower than with intracellular access.

In the following section we establish a simulation methodology amenable to investigate the impact of electrode morphology and material on the expected electrical transduction performance of the sensors

3. Methodology

The review in Section 2 suggests that comprehensive models of the neuron-sensor interface, aimed at studying the transduction mechanisms of electrophysiological signals, should be

#	N. sites	Pitch	Access mean	Type	Rec. time/DIV	Max ampl.	SNR Max	Ref.	Pub. Year
1	>1	8 μm	extracellular mushroom	passive	>1min/>2	20mV	333*	[35] [36]	2015
2	65536	25.5 μm	extracellular planar	active	12s/n.a.	120 μV	70	[33]	2017
3	1-20	2-5 μm	intracellular optoporation	passive	80min/3	1.8mV	30*	[38]	2017
4	64	4 μm	intracellular spontaneous	passive	>3min/>2	99mV	1700	[44]	2017
5	168	2 μm	intracellular biochemical	active	>3min/14	100mV	144	[48]	2019
6	4096	20 μm	intracellular electroporation	active	19min/4	10mV 1nA	167* 333*	[39]	2019
			extracellular nanowire	active	20min/12	62 μV 93pA	<10 >10	[42]	2020
7	59	200 μm	extracellular mushroom	passive	>30min/35	550 μV	31*	[37]	2020

Table 2. Performance comparison of different recording systems. When not directly accessible from the papers, the SNR has been calculated as $V_{out}[V_{pp}]/3V_{n,out}[V_{rms}]$, following [48] and marked with * in the table. $V_{out}[V_{pp}]$ is the peak-to-peak value of the recorded AP, while $V_{n,out}[V_{rms}]$ is the rms value of the output noise. The numbers in the first column refer to: 1= Gold mushroom micro-electrode, 2= MEA, 3= Plasmomic nanowire, 4= High aspect-ratio nanowire, 5= U-shaped FET, 6=CNEA, 7=PEDOT:PSS-coated gold mushroom micro-electrode. DIV refers here to consecutive Days of In-Vitro experiments.

multiphysics, multiscale, and capable to treat electrical signal generation and propagation across complex three dimensional structures, made of diverse materials, including active semiconductor devices, passive interconnects, and electrodes in contact with electrolytes. A co-integration with flexible probes is also possible but the extension of the proposed methodology to this type of sensor falls outside the scope of this work. Therefore, having in mind the perspective of sensing devices integrated in CMOS technology, a natural choice is to rely on Technology Computer Aided Design tools (TCADs) (e.g., SDevice [53]) as an alternative to general multiphysics simulation packages (e.g., COMSOL®). In this work we embrace the first choice. SDevice solves self-consistently the semiconductor equations (Poisson, continuity and drift-diffusion equations) in non-linear steady state and transient regimes using the Finite Element Method (FEM). It also performs small signal AC and noise analysis. In addition, it can couple physical structures described with the FEM to electrical circuits described by netlists thanks to a mixed-mode device-circuit simulation capability [53].

The TCAD does not yet incorporate general electrolyte physics directly but, exploiting the similarity of electrons and holes in semiconductors to anions and cations, and tailoring the permittivity, mobility, bandgap, effective density of states and affinity of a generic-semiconductor, the electrolyte medium can be modelled [54–56]. A physical model interface (PMI) [57] allows users to add models for surface chemical reactions, whereas the formation of electrical double layers at charged surfaces stems naturally from the drift-diffusion transport framework. The main limitations of this approach, and possible workarounds, have been examined in [55] and will not be repeated here. Section (a) of the Additional information provides the parameter values adopted in our calculations.

At first order, pristine cellular membranes can be described as a lossless insulating layer [58] with a relative permittivity and a capacitance equal to those of the biological neuronal membrane ($\epsilon_{r,mem} \approx 11$, $C_m \approx 1 \mu\text{F}/\text{cm}^2$, respectively [59]). To model the electrogenic functions of the

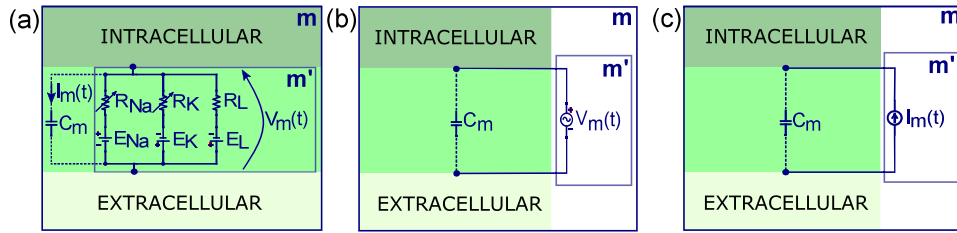


Figure 2. Schematic representation of mixed-mode approaches to introduce in the TCAD the action potential generation mechanisms across the insulating layers representing at first order the cellular membranes: (a) Hodgkin-Huxley model [61], (b) voltage source as external boundary condition, (c) ionic transmembrane current source. (b) and (c) are simpler approximate versions of (a). In the TCAD FEM domain the membrane capacitance C_m is not a lumped element but it results from the solution of Poisson's equation in the insulating layer. The primed blocks (e.g., m') represent the external lumped elements to add to the TCAD; m blocks, instead, represent the combination of C_m and m' .

biological neuron, we proceed as follows. Firstly, we discretize the membrane in compartments [18,60]. Then, we introduce small contacts on both sides of the compartments' membrane and connect between them appropriate lumped circuit components. To emulate the AP and related transmembrane current, for each compartment we connect one of the primed blocks suggested in Fig. 2. The Hodgkin-Huxley (HH) model (Fig. 2.a, [61]) accounts for the non-linear, voltage-dependent and time-varying nature of the ion channels across the membrane. In this work we use the time-invariant version of the HH [62–64] and adopt the ion concentrations for humans [65] to compute the equilibrium voltage generators (E_K , E_{Na} , E_L), although any signal generation mechanism amenable to a lumped-element SPICE-like description could be used as well thanks to the mixed-mode device-circuit simulation environment adopted in this work. The HH model should be instantiated for each compartment (a single one is shown in Fig. 2.a). Alternatively (see Fig. 2.b), an independent voltage generator can be used, imposing the same AP waveform $V_m(t)$ of the HH model (which accounts for the -70 mV physiological rest membrane potential) as an external boundary condition between the compartment contacts. This simple approach is adequate only when simulating *intracellular* sensing [58], as further discussed in the description of Fig. 4. Yet another possibility, Fig. 2.c, is to use an independent transmembrane current generator, I_m , imposing the same total current flowing through the HH model's membrane capacitance, C_m in Fig. 2.a. In this case, the physiological rest membrane potential is imposed as initial condition to the capacitor voltage and thus added to the AP waveform. This last solution, inspired by [19], is best suited to describe *extracellular* sensing, since it grasps the distributed nature of the I_m and, in principle, can be scaled to an arbitrarily fine compartmentalization of the membrane.

In this work, simulations will consider three compartments per neuron, chosen consistently with Fig. 1 and [19], in order to represent: 1) the average behavior of the nano-junctional membrane area where intimate coupling between the neuron and the sensor is achieved (subscript njm); 2) the junctional portion of the membrane in proximity of the njm compartment, that can still couple some signal to the sensor device (subscript jm); 3) the non-junctional portions of the membrane, far from the sensing device, which can affect the response by introducing parasitic leakage paths (subscript nm). The lumped element values for each compartment must be scaled proportionally to the respective estimated membrane area: $A_{njm}/A_m=4\%$, $A_{jm}/A_m=19\%$, $A_{nm}/A_m=77\%$, $A_m=220\ \mu\text{m}^2$ in the following [19].

For intracellular contact of the sensor, the njm compartment is replaced by a single resistor, because an electroporated membrane is reported to behave as a $400\ \text{M}\Omega$ to $18.8\ \text{G}\Omega$ resistance with negligible capacitance nor HH blocks in parallel [39]. An intermediate $R_{njm}\simeq 2\ \text{G}\Omega$ has been chosen in this work, consistent with [19]. Alternatively, poration can be described at the physical level by introducing gaps in the membrane insulating layer in the FEM mesh.

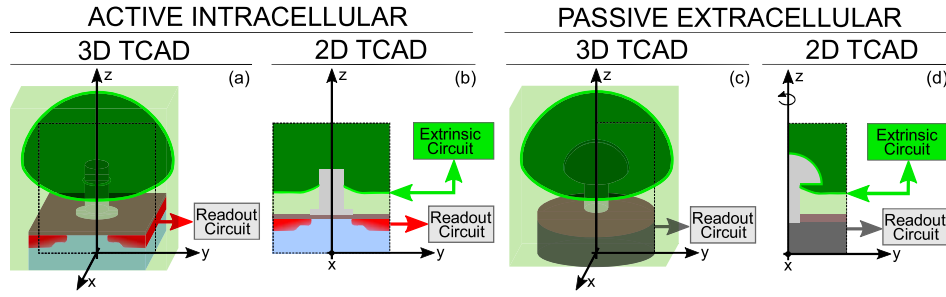


Figure 3. Schematic representation of the sensor system considered in this work and corresponding simulation setups. (a) and (c) sketch full 3D TCAD domains connected to readout circuits. The neuron soma is represented as a circular dome. The sensing elements are: (a) an active intracellular needle; (c) a passive extracellular mushroom shaped electrode with cylindrical symmetry around the z -axis. (b) and (d) represent the mixed-mode 2D TCAD-circuits corresponding to the full 3D TCAD domains. The *intrinsic* njm 2D domain inside the dashed box is still solved with FEM but the *extrinsic* part of the domain and the readout are accounted for by lumped element circuits.

Fig. 3 schematically represents the simulation domains investigated for two reference case studies developed in Section 4 (namely, an active intracellular sensor and a passive extracellular sensor) treated at different abstraction levels: full 3D-TCAD domains, (a)(c), or as mixed-mode combinations of 2D-TCAD and circuits, (b)(d). The readout is always represented as a circuit. The neuron soma is sketched as a 3D dome; the needle sensor in (a)(b) retains the rectangular symmetry of the underlying FET while the passive-extracellular mushroom-shaped nanoelectrode, inspired by the work of [27,35], has cylindrical symmetry (c)(d).

Owing to symmetry, the 3D domain can be approximated to 2D (Figs. 3.b and 3.d) still retaining the essence of the full 3D descriptions and provided the simulations are run in rectangular and cylindrical coordinates, respectively. Among the many possible combinations, in the following we describe the FET at the circuit level, which allows to use cylindrical coordinates for both the needle and the mushroom protrusions. The *extrinsic* parts of the system, i.e., the ones that are not directly part of the sensing elements and thus are not included in the FEM domain, are modelled by an equivalent circuit. Our previous work [58] suggests that an RC (i.e., resistors and capacitors) circuit representation with few lumped elements, neglecting the distributed nature of these domains, is adequate if clefts are sufficiently conductive.

Fig. 4 shows the simplified lumped elements equivalent circuit representations of the TCAD structures in Fig. 3, compartmentalized in three sections. The first row sketches two types of nano-electrode/neuron interface with intra- (left) and extra- (right) cellular access. The njm', jm' and nm' rectangles represent one of the possible options in Fig. 2 to include the generation of the AP and are treated as open circuits during frequency domain analysis, as discussed at the end of this Section.

The dashed rectangles in the first row of Fig. 4 contain the circuits that represent the finite element simulation domain in Fig. 3.b and d (i.e., C_{njm} , C_{nano} , R_{nano}). The lumped elements values are estimated with simple formulas for resistance and capacitance of cylindrical and rectangular structures [18,58], and are consistent with [35,44], as reported in Tab. A1 of the Additional information. The components of the extrinsic part of the domain (i.e., R_{njm} , R_{njseal} , C_{jm} , C_{nm} , R_{jseal} , C_{pad} , R_{stray} , C_{stray} , g_m , R_{feed} , R_2 , R_1) are common to both mixed-mode TCAD (Fig. 3) and full circuit simulations (Fig. 4). Their values are reported in Tab. A1 of the Additional information as well.

The circuits in the second row of Fig. 4, instead, represent the essence of the readout for the passive (left) and active (right) sensors. The former is a voltage-amplifier with low frequency gain $(1+R_2/R_1)$. The active sensing circuit, instead, embeds an OpAmp-based transimpedance-amplifier to convert the FET drain current into an output voltage. The gain is set by R_{feed} and is chosen to ensure the same peak-to-peak signal amplitude of the passive sensing case under good

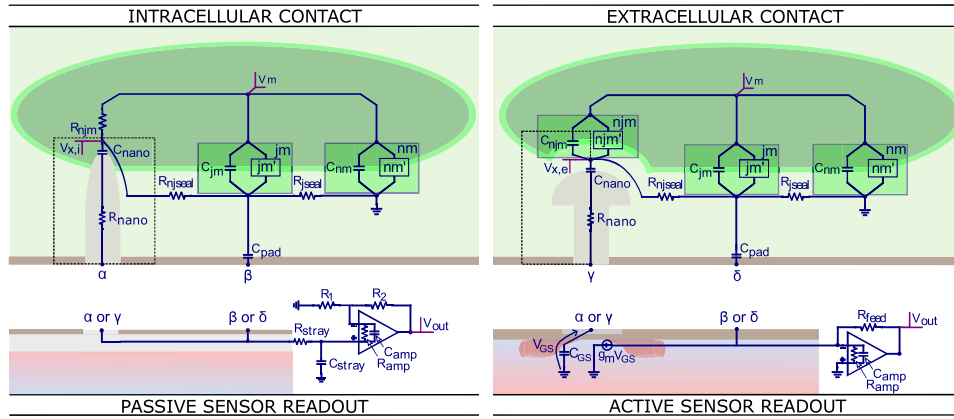


Figure 4. Essential equivalent circuit representation of the TCAD models in Fig. 3 used to compute the AP transients, the transfer function $\mathcal{H}(f) = V_{out}(f)/V_m(f)$, and the noise. The dashed rectangles enclose the equivalent circuit representation of the 2D TCAD portions of Fig. 3. Both the intracellular needle contacts (α and β , top-left) and the extracellular mushroom contacts (γ and δ , top-right) can be connected either to the passive (bottom-left) or to the active (bottom-right) readout circuits. R_{njm} is the resistance of the cytosol between the bulk of the intracellular electrolyte at potential, V_m , and the tip of the nano-electrode; C_{njm} , C_{jm} , and C_{nm} represent the series of diffusion-Stern-membrane-Stern-diffusion capacitances of the neuron compartments in Fig. 1; R_{njseal} and R_{jseal} are the nano-junctional and junctional sealing resistances; C_{nano} is the series of the Stern and EDL capacitances of the cytosol/electrolyte on the surface of the nano-electrode; R_{nano} is the nano-electrode resistance; C_{pad} is the insulator capacitance between the extracellular electrolyte and the planar portion of the electrode; R_{stray} and C_{stray} account for the parasitic resistance and capacitance of the connections to the readout; R_2 and R_1 set the passive readout gain; g_m is the FET transconductance; R_{feed} sets the active readout gain; R_{amp} and C_{amp} are the input resistance and capacitance of the operational amplifier employed in the readout circuit. C_{GS} is the FET Gate to Source capacitance.

sealing conditions, i.e., high nano-junctional sealing resistance ($R_{njseal}=900 \text{ M}\Omega$). These R_{feed} values are then kept constant for the poor sealing conditions as well ($R_{njseal}=100 \text{ M}\Omega$).

Different circuit blocks from Fig. 2 are inserted in the njm' , jm' and nm' rectangles according to the required type of simulation. The default choice in this work has been to replace all of them with the HH block (Fig. 2.a) when simulating the AP transient response. However, reasonably accurate results have been obtained with simpler choices. In particular, for *intracellular recording* (top left in Fig. 4) we placed a voltage source of the AP waveform $V_m(t)$ inside the nm' rectangle (as in Fig. 2.b) and treat as open circuit the rectangle nj' . This is an adequate solution as long as the intracellular neuron potential is essentially uniform over the volume directly sensed by the nano-electrode. When simulating transients for *extracellular recording*, instead, a set of $I_m(t)$ current sources as in Fig. 2.c has been introduced into the three rectangles: $I_{njm}(t)$ in njm' , $I_{jm}(t)$ in jm' , and $I_{nm}(t)$ in nm' . This is because the extracellular ionic currents and related potentials change from one compartment to another depending, above all, on ion channel distributions and sealing conditions. The $I_{njm}(t)$, $I_{jm}(t)$ and $I_{nm}(t)$ waveforms replicate the currents flowing through the C_{njm} , C_{jm} , C_{nm} of a neuron described by the HH model (Fig. 2.a) once partitioned into these three compartments in circuit simulations.

When performing linearized AC small signal analysis, for both intracellular and extracellular recording we place an AC voltage source between node V_m and ground, and open all the circuits inside the rectangles (njm' , jm' , nm') of Fig. 4. Thus, only the capacitances are retained within the compartments, which is a good approximation when the AP has not started yet [19]. The resulting circuits are used to extract the system transfer function $\mathcal{H}(f) = V_{out}(f)/V_m(f)$, compute the thermal noise of the sensor, and then the signal-to-noise ratio (SNR), as will be discussed in Section 4.

The composite model outlined above combines numerical FEM simulations with a set of previously defined circuit models that rely on parameter values validated either by experiments, or, in a few instances, by TCAD simulations. In particular, the time-invariant HH model with compartmentalization has been used in [18,60], and in [19] in its transmembrane current-sources version; the model for the neuron-electrode junction is consistent with [17,29]. Concerning the value of the circuit components used in the models: R_{njm} is taken from the experiments in [66], later confirmed by [39]; R_{njseal} has been taken from [19] that slightly modified the value from the experiments in [66]; R_{jseal} is computed as the disk resistance given the cleft thickness, and the hole and rim ring radii according to Eq. (11) in [18]; C_{njm} , C_{nm} , C_m , are the capacitances obtained by scaling the value $C_m=2.2$ pF [19] according to the relative area of the different portions of the membrane based on the geometry of the system; C_{nano} is computed according to the third expression in Tab. 2 of [58], where the area is given by Eq. (7) of [18] possibly adding the contribution of the cap for mushroom shaped sensors; R_{nano} is computed according to Eq. (8) in [18] with or without the mushroom cap, as appropriate; C_{pad} is computed according to the fourth formula in Tab. 2 of [58]; R_{stray} and C_{stray} have been computed according to the last two expressions in Tab. 2 of [58], employing the formulas for parallel plate capacitor and barrel resistor using realistic values for the geometry of the interconnects; R_{amp} and C_{amp} are the input resistance and capacitance of a typical OpAmp (taken from [19]); the g_m of the active sensor is taken from [75] and refers to a realistic advanced 28nm CMOS node. C_{njm} , C_{nano} , and R_{nano} have been also verified by means of TCAD simulations (as we will see later in Section 4(b)).

Our general purpose model can be adapted to a variety of sensor implementations by tuning the parameter values on adequate experiments or TCAD simulations. In the following it will be used to highlight trends of general validity which are modestly affected by the specific parameter values, and to investigate the relation between sensor morphology, circuit elements, and expected performance.

4. Results

(a) Physics-based TCAD simulations of action potential transients

The use of the TCAD enables to relate the geometrical/physical and material sensor parameters to the shape of the recorded signal without need to rely upon equivalent circuits or analytical formulas. Fig. 5 shows the expected impact of changes in these parameters for nano-electrodes (e.g., the height, H , and diameter, D , of a nanowire; the mushroom's cap diameter, D , and stalk height, H , while keeping constant the cap's height, 658 nm, and the stalk diameter, 554 nm), and materials (Pt or doped Silicon), whose specific values are given in the caption. Note that the output signals are plotted as variation with respect to the DC value, so all waveforms start from and tend to zero volts.

Fig. 5 points out that active sensors (open symbols) are essentially insensitive to the size and material of the nano-electrode, whereas the choice of relatively large nano-electrodes, possibly made of metal conductors, is mandatory to increase the performance of passive sensors (filled symbols). To compare the different solutions, in the following of this work we keep Platinum as reference material for nano-electrodes, with default dimensions H_2, D_2 (see caption of Fig. 5 for specific values).

(b) Physics-based TCAD vs equivalent circuit representations

To validate the equivalent circuit representation of the recording system in Fig. 4 and the chosen lumped element values (Tab. A1 in the Additional) we compare the transient response computed with the circuit to the one computed with mixed-mode TCAD simulations of the 2D physical domains in Fig. 3.

Fig. 6 compares these simulations under the assumption of good sealing conditions ($R_{njseal}=900$ M Ω), and demonstrates a very good agreement in all cases. The sources of the AP

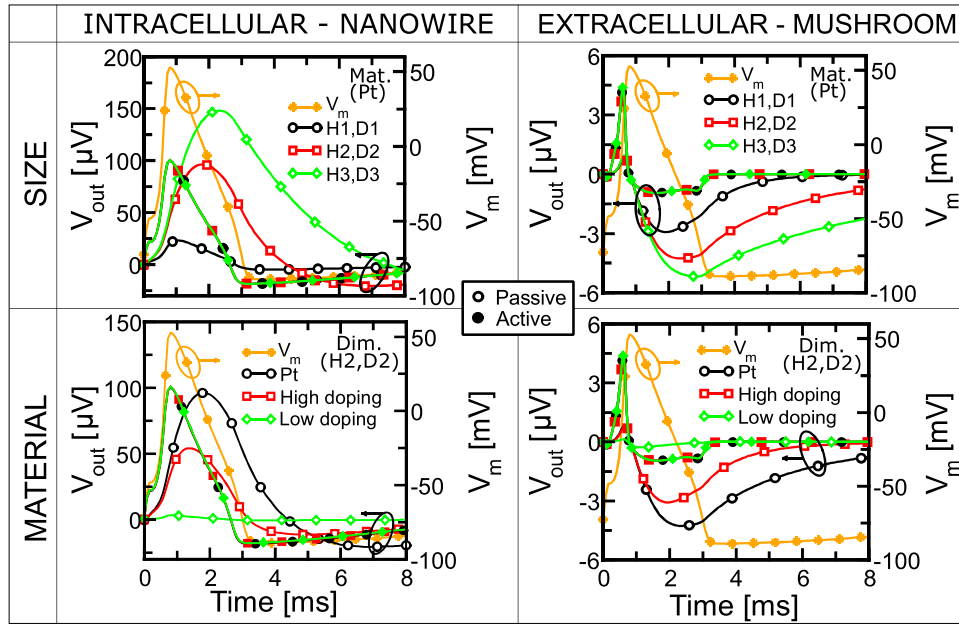


Figure 5. Transient response to an AP recorded by active (filled symbols) or passive (open symbols) in TCAD for the structures in Fig. 3, for different devices (intracellular nanowire, left column; extracellular mushroom, right column), materials (Platinum, lowly doped Silicon, $5 \cdot 10^{16} \text{ cm}^{-3}$ and highly doped Silicon, $5 \cdot 10^{19} \text{ cm}^{-3}$) and sizes (Nanowire's height and diameter: $H1 = 1 \mu\text{m}$, $D1 = 250 \text{ nm}$ / $H2 = 3.8 \mu\text{m}$, $D2 = 554 \text{ nm}$ / $H3 = 5 \mu\text{m}$, $D3 = 1.5 \mu\text{m}$; Mushroom's stalk height and cap diameter: $H1 = 685 \text{ nm}$, $D1 = 250 \text{ nm}$ / $H2 = 1.13 \mu\text{m}$, $D2 = 2 \mu\text{m}$ / $H3 = 3 \mu\text{m}$, $D3 = 3 \mu\text{m}$, with cap's height and stalk diameter fixed respectively at 658 nm and 554 nm). The reference material when analysing size effects (top row) is Platinum; whereas the default dimensions when varying materials (bottom row) is H2,D2. The sources of the AP waveform are implemented as a single voltage generator for intracellular contact, vs three current generators, one per compartment, for extracellular contact, as described in Section 3. V_{out} is reported as variation with respect to the DC value.

waveform (rectangles in Fig. 4) are implemented as described in Section 3 for both TCAD and circuit simulations. V_{out} is reported as variation with respect to the DC value; again all waveforms start from and tend to zero volts. This analysis validates the C_{njm} , C_{nano} , R_{nano} values estimated from the TCAD and allows us to employ the circuit representation of Fig. 4 in the following.

(c) Transient response to action potentials and Transfer Functions

Fig. 7 shows the AP waveforms recorded at the output node of the passive and active sensor circuits in Fig. 4 for different sealing conditions. Also in this case the sources of the AP are implemented as described in Section 3. All the signals captured with *intracellular* contact have a monophasic profile, resembling in many cases an attenuated replica ($V_{pp} \approx 120 \mu\text{V}$) of the intracellular AP for both passive and active sensors with good neuron sealing (left column). The reason why, in the passive case, the intracellular V_{out} differs from an attenuated replica of the neuron AP will be explained later by means of the transfer function analysis. The signal reduces to $\approx 20 \div 30 \mu\text{V}_{pp}$ if sealing is less effective (right column), highlighting the importance of good adhesion of the neuron to the sensor. On the other hand, the signals sensed with *extracellular* contact have a biphasic shape, resembling the first time derivative of the intracellular AP. The V_{pp} is much smaller than its intracellular counterpart, and therefore it is magnified in the figure. Approximately, both passive and active sensors achieve $\approx 6 \mu\text{V}_{pp}$ with $R_{njseal} = 900 \text{ M}\Omega$, and $\approx 1 \mu\text{V}_{pp}$ or less with $R_{njseal} = 100 \text{ M}\Omega$. While these numbers depend on the chosen parameter values

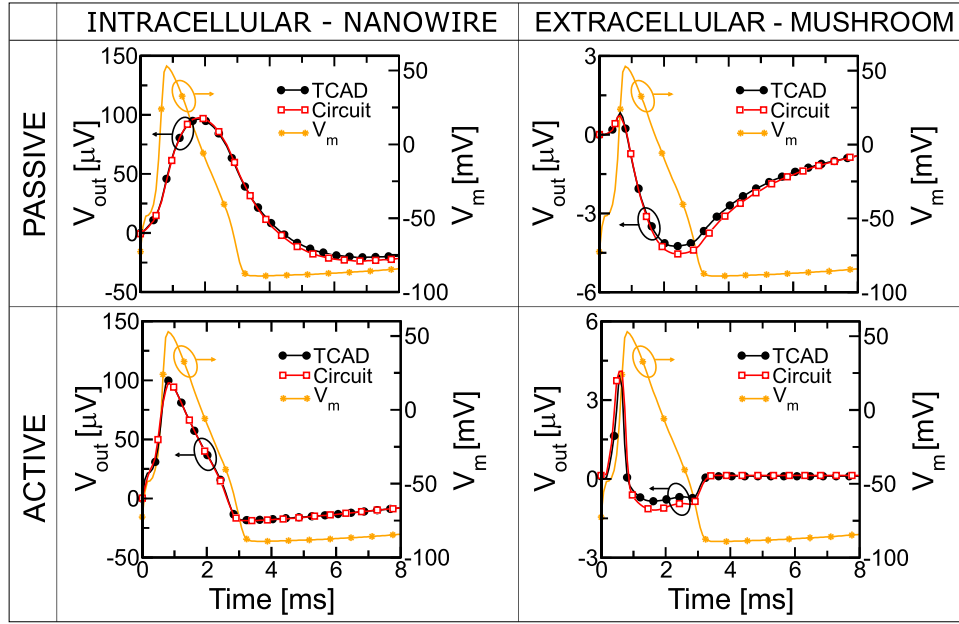


Figure 6. Transient response to an AP computed according to the TCAD (Fig. 3) and the lumped element circuit (Fig. 4) models for passive (top row) and active (bottom row) intracellular (left column) and extracellular (right column) recording systems under good sealing conditions ($R_{njseal}=900 \text{ M}\Omega$). The sources of the AP waveform (rectangles in Fig. 4) are implemented as described in Section 3 for both TCAD and circuit simulations (single voltage generator for intracellular vs three current generators, one per compartment, for extracellular). V_{out} is reported as variation with respect to the DC value.

and can be improved to some extent by changing the sensor geometry and coupling to the neuron, the observed trends are consistent with expectations because of the screening of the double layers at the cleft's interfaces in the intrinsic part of the device next to the protrusions and because of the fact that R_{jseal} is directly connected to ground.

With the goal in mind to investigate the time and frequency responses of the four case-study systems of Fig. 6 for various neuron-sensor coupling conditions, Fig. 8 shows the modulus of the transfer functions (TFs) $|\mathcal{H}(f)| = |V_{out}(f)/V_m(f)|$ for the circuits in Fig. 4 and two R_{njseal} values over an extended frequency range suited to identify some relevant features. Qualitatively speaking, the TFs confirm that in the frequency range of the AP spectra, a flat gain can be achieved in *intracellular* sensing conditions, whereas for *extracellular* sensing the TFs are dominated by low frequency zeros. This is the reason why for intracellular sensing the output waveform resembles an undistorted and scaled copy of the AP, while for extracellular sensing it reflects the distorted time derivative of the AP.

To further discuss these aspects, we write the transfer function in the rational form:

$$|\mathcal{H}(f)| = G_{in-band} \left(\frac{f}{f_0} \right)^k \frac{(1 + jf/f_{z1})(1 + jf/f_{z2})(\dots)(1 + jf/f_{zn})}{(1 + jf/f_{p1})(1 + jf/f_{p2})(\dots)(1 + jf/f_{pn})}, \quad (4.1)$$

where $G_{in-band}$ is the in-band gain, k is the number of zeros in the origin, and $f_{z1}, f_{z2}, \dots, f_{zn}, f_{p1}, f_{p2}, \dots, f_{pn}$ are the zero and pole frequencies, respectively. Following similar steps as in [58], we used open and short circuit time constants analysis [67] to determine approximate analytical formulas for the poles, zeros and in-band gain of the $\mathcal{H}(f)$ (see Tab. 3) as a function of the lumped element parameter values reported in Tab. A1; the availability of free-distribution codes (e.g., SCAM [68]) could yield exact analytical expressions given the circuit topology. To this end, the FET capacitances (C_{GS} , etc.) have been neglected, since they are much smaller than the other

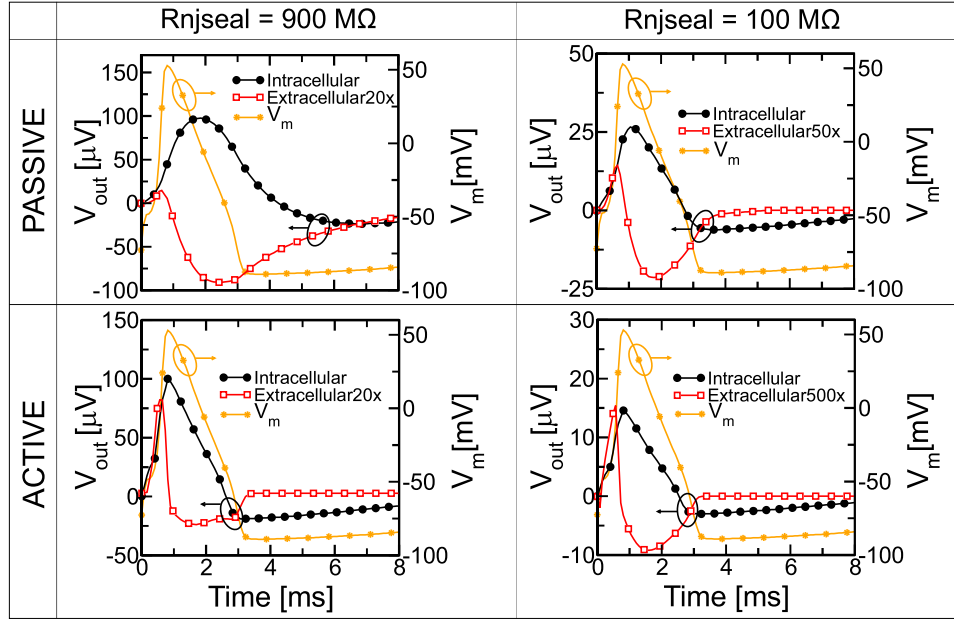


Figure 7. Action potential waveforms recorded at the output node of the passive and active sensing circuits in Fig. 4 for different sealing conditions. The sources of the AP waveform (rectangles in Fig. 4) are implemented as described in Section 3 (single voltage generator for intracellular vs three current generators, one per compartment, for extracellular). Extracellular contact waveforms are magnified for improved visibility.

capacitances. Some poles and zeros lie outside the frequency range of AP spectrum of Fig. 8; their expressions are reported in Tab. 3 as well. The order adopted in the table reflects increasing frequency for chosen parameter values, i.e., $F_{z,i} < f_{z,i+1}$ and $F_{p,i} < f_{p,i+1}$.

In the following, we provide a short description of the transfer function for each case.

(a) Intracellular-passive sensor: the TF has two zeros, one in the origin ($k=1$) and one in the MHz regime (Eq. (4.3) in Tab. 3, thus not visible in Fig. 8), and four poles. The low frequency f_{p1} and f_{p2} shape the bandwidth as depicted in the top-left graph of Fig. 8. The remaining poles fall above the upper frequency limit of the figure (Eqs. (4.6) and (4.7) in Tab. 3). The in-band gain is set by capacitive and resistive dividers according to Eq. (4.2) in Tab. 3. To maximise the gain and reduce distortion (i.e., to widen the flat portion of the TFs by making f_{p1} small and f_{p2} high), R_{amp} , R_{njseal} and C_{nano} should be large, and C_{stray} and C_{amp} small according to Eqs. (4.4) and (4.5). In fact, a low f_{p2} (e.g., for large values of the sealing resistance) filters out the high-frequency signal components, thus slowing the V_{out} transients and making it appear spread out over time (black line in the top-right panel of Fig. 7). As a result, the recorded signal is not a pure scaled replica of the intracellular signal. This lowpass effect is mitigated for low sealing resistance which widens the bandwidth (top-right panel of Fig. 8) and makes the V_{out} follow the V_m profile more closely (top-right panel of Fig. 7), although with lower amplitude because of the reduced in-band gain.

(b) Extracellular-passive sensor: the TF has two zeros in the origin ($k=2$) and four poles. The pole at f_{p2} sets the lower cut-off frequency of the bandwidth. The third and fourth poles lie beyond the upper limit of Fig. 8 (Eqs. (4.12) and (4.13) in Tab. 3). The in-band gain is given by Eq. (4.9) and increases if C_{njm} and C_{jm} are large, and C_{stray} and C_{amp} small. Because of the double zero in the origin, conventional extracellular sensors record signals that resemble the first time-derivative of the intracellular potential only if f_{p1} is small (thus compensating one zero) and f_{p2} is large. If f_{p2} is low, the recorded signal is a sort of derivative of the AP but spread over time due to the additional low-pass nature of the system. This lowpass effect can be mitigated for small

Passive Intracellular	
$G_{in-band}$	$\left(\frac{R_{njseal} + R_{jseal}}{R_{njseal} + R_{jseal} + R_{njm}} \right) \left(\frac{C_{nano}}{C_{nano} + C_{pad} + C_{stray} + C_{amp}} \right) \left(1 + \frac{R_2}{R_1} \right)$ (4.2)
f_{z1}	$\frac{1}{2\pi C_{njm} R_{jseal} (1 + R_{njm}/R_{njseal})}$ (4.3)
f_{p1}	$\frac{1}{2\pi (C_{nano} + C_{pad} + C_{stray} + C_{amp}) R_{amp}}$ (4.4)
f_{p2}	$\frac{1}{2\pi (R_{njseal}/R_{njm} + R_{nano} + R_{stray})} \left(\frac{1}{C_{nano}} + \frac{1}{C_{amp} + C_{stray}} \right)$ (4.5)
f_{p3}	$\frac{1}{2\pi} \left(\frac{1}{C_{nano} R_{njseal}/R_{njm}} + \frac{1}{C_{pad} R_{stray}} \right)$ (4.6)
f_{p4}	$\frac{1}{2\pi} \left(\frac{1}{C_{jm} R_{jseal}} + \frac{1}{C_{nano} R_{njseal}/R_{njm}} \right)$ (4.7)
BW	$f_{p1} < f < f_{p2}$ (4.8)
Passive Extracellular	
$G_{in-band}$	$\frac{C_{njm}}{C_{stray} + C_{amp}} + \frac{C_{jm}}{C_{stray} + C_{amp}} \frac{R_{jseal}}{R_{jseal} + R_{njseal}} \left(1 + \frac{R_2}{R_1} \right)$ (4.9)
f_{p1}	$\frac{1}{2\pi (C_{nano} + C_{pad} + C_{stray} + C_{amp}) R_{amp}}$ (4.10)
f_{p2}	$\frac{1}{2\pi (R_{njseal} + R_{jseal} + R_{nano} + R_{stray})} \left(\frac{1}{C_{nano}} + \frac{1}{C_{amp} + C_{stray}} \right)$ (4.11)
f_{p3}	$\frac{1}{2\pi (C_{njm} + C_{pad}) R_{stray}}$ (4.12)
f_{p4}	$\frac{1}{2\pi R_{nano}} \left(\frac{1}{C_{njm}} + \frac{1}{C_{nano}} + \frac{1}{C_{pad}} \right)$ (4.13)
BW	$f > f_{p2}$ (4.14)
Active Intracellular	
$G_{in-band}$	$\left(\frac{R_{njseal} + R_{jseal}}{R_{njseal} + R_{jseal} + R_{njm}} \right) g_m R_{feed}$ (4.15)
f_{z1}	$\frac{1}{2\pi C_{njm} R_{jseal} (1 + R_{njm}/R_{njseal})}$ (4.16)
f_{p1}	$\frac{1}{2\pi C_{jm} R_{jseal}}$ (>10 kHz in Fig. 8) (4.17)
f_{p2}	Related to the OpAmp GBW (>10 kHz in Fig. 8) (4.18)
BW	$f < f_{p1}$ (4.19)
Active Extracellular	
$G_{in-band}$	$g_m R_{feed}$ (4.20)
f_{p1}	$\frac{1}{2\pi C_{njm} R_{njseal}}$ (>1 kHz in Fig. 8) (4.21)
f_{p2}	Related to the OpAmp GBW (>10 kHz in Fig. 8) (4.22)
BW	$f_{p1} < f < f_{p2}$ (4.23)

Table 3. Approximate expressions of the in-band gain, poles, and useful bandwidth of the system transfer functions, $\mathcal{H}(f)$, represented in Fig. 8. C_{njm} and C_{jm} are much lower than $C_{stray} + C_{amp}$ for our case study.

R_{njseal} paying the penalty of a slightly-reduced in-band gain. Furthermore, by looking at Eqs. (4.10) and (4.11), we deduce that R_{amp} and C_{nano} should be large, and C_{stray} and C_{amp} small. On the other hand, to faithfully record signals with undistorted intracellular-like waveforms, constant gain and linear phase [67] should be achieved over the whole frequency range of the AP, and not only at its upper edge as visible in the figure. The f_{p2} should approach f_{p1} ($<0.1\text{Hz}$), e.g., by maximizing R_{njseal} , consistently with the experimental evidence in [28] where $G\Omega$ of sealing resistance are reported.

(c) Intracellular-active sensor: the TF features one zero (Eq. (4.16)) and two poles in the MHz range ($k=0$), hence not visible in Fig. 8, that cut-off the useful frequency bandwidth. The f_{p1} depends on the $C_{jm} R_{jseal}$ product (see Eq. (4.17)), while the large gain-bandwidth product of the OpAmp, (GBW=5 MHz in our simulations) controls f_{p2} . As a result, high frequency distortion in the useful frequency spectrum disappears. Moreover, the bandwidth extends toward very low frequencies ($<1\text{ mHz}$) which is an interesting feature to monitor slowly varying neuronal signals such as subthreshold potentials and membrane oscillations (see Tab. 1). As a result, the recorded signal represents a non-distorted scaled replica of the intracellular AP. However, if not otherwise limited, such a large bandwidth collects excessive noise and reduces the SNR, as discussed in more detail in the following section. Notice that, if the C_{GS} of the FET is negligible, as in this case, the capacitive divider $C_{nano}/(C_{nano} + C_{GS}) \approx 1$; hence, it does not affect the in-band gain. The $G_{in-band}$ value is then set by the resistive divider as per Eq. (4.15) and can be maximized by making R_{njseal} , g_m , and R_{feed} large and R_{njm} small.

(d) Extracellular-active sensor: the TF has one zero in the origin ($k=1$) and two poles which shape the bandwidth according to Eqs. (4.21) and (4.22), respectively. The in-band gain is set by the $g_m R_{feed}$ product (see Eq. (4.20)) which should then be large. Conventional extracellular sensors require large f_{p1} and f_{p2} to maintain the characteristic derivative behavior (i.e., the sloped straight line in Fig. 8, bottom left panel, over most of the AP spectrum frequency range). Thus, R_{njseal} and C_{njm} should be small and the OpAmp GBW should be large, although a reduced gain with poor sealing may effectively prevent signal detection. Conversely, for intracellular-like sensors f_{p1} should be small ($<0.1\text{ Hz}$); this requires a large R_{njseal} yielding to the same conclusions as for the extracellular passive sensor case.

All these observations elucidate how the actual neuron waveform transduced by the sensor is subject to considerable uncertainty since the transfer function is sensitive to the actual quality of the contact, the ratio between nano-junctional, junctional and non-junctional portions of the membrane, and the sealing. The applicability limit of the TFs to the analysis of AP transient is examined in Section (c) of the Additional information.

(d) Comparison with transfer functions from literature

It is instructive to compare our transfer function calculations in Tab. 3 to those reported (only for extracellular passive planar MEA sensors) in [69,70]. Since our model has additional features with respect to [69,70] (for instance: three compartments instead of the two, the inclusion of the readout which is not accounted in [69]), a few assumptions and adaptations are necessary for meaningful results: 1) our three-compartment model (which refers to a protruding-nano-electrode and thus describes the nano-junctional interaction with the neuron) has been reduced to a two-compartment model for planar electrode as in [69,70] by making R_{njseal} negligible w.r.t. R_{jseal} ; 2) the electrode is assumed ideally polarizable and free of Faradaic currents. Consequently we set $R_e = \infty$ in the model of [69]. 3) A perfect overlap of the neuron onto the electrode is assumed and thus we set $C_{dl}'' = 0$ in the model of [70]. The full correspondence between the models' parameters is described in the caption of Tab. 4.

The result of the comparison is reported in Tab. 4 in terms of analytical transfer functions and in Fig. 9 in terms of $|\mathcal{H}(f)|$. The main differences between the three models are summarized as follows: 1) all the models have the same f_{p2} (Eqs. (4.30)(4.31),(4.32)); 2) the model of this work accounts for the interconnect parasitics and readout circuit (C_{stray} , R_{amp} and C_{amp}) which generate an additional low-frequency pole, f_{p1} (Eq. (4.27)), accounted for in [70] (Eq. (4.29)) but

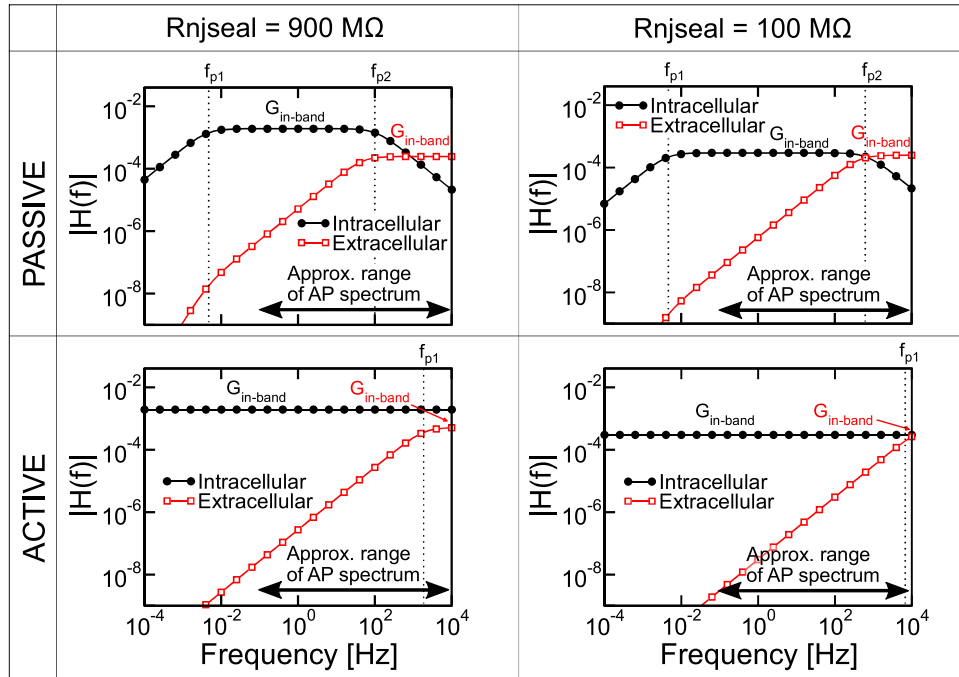


Figure 8. Modulus of the system transfer function $|H(f)| = |\mathcal{V}_{out}(f)/\mathcal{V}_m(f)|$ of the passive and active, intracellular and extracellular sensing systems in Fig. 4 for different sealing conditions. Poles and in-band gains are specified inside the graphs; their expressions are listed in Tab. 3 in the Additional information.

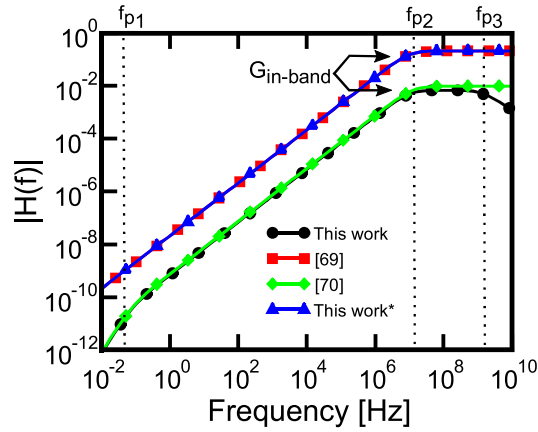


Figure 9. Comparison of the transfer function modulus for the extracellular passive sensor vs calculations in [69] and [70]. Poles and in-band gains are specified inside the graphs; their expressions are listed in Tab. 4. The expression marked as **This work*** was found eliminating the effect of R_{nano} , R_{stray} , C_{stray} , C_{amp} , R_{amp} from the original circuit.

not in [69]; 3) only our model predicts the presence of an additional cut-off frequency, f_{p3} (Eqs. (4.33)), due to the components such as R_{stray} , C_{pad} and the nano-junctional membrane, C_{njm} , which may pose additional limitations to the bandwidth depending on the parameter values; 4)

$G_{in-band}$	
[This work]	$\frac{C_{njm}}{C_{stray} + C_{amp}} + \frac{C_{jm}}{C_{stray} + C_{amp}} \frac{R_{jseal}}{R_{jseal} + R_{njseal}} \left(1 + \frac{R_2}{R_1}\right) \quad (4.24)$
[69]	$\frac{C_{hd}}{C_{hd} + C_e} \quad (4.25)$
[70]	$\frac{C'_{jm}}{C_{lsh} + C_{ain}} + \frac{C_m}{C_{lsh} + C_{ain}} \frac{R_s}{R_{jseal} + R_{jseal}} \left(1 + \frac{R_2}{R_1}\right) \quad (4.26)$
f_{p1}	
[This work]	$\frac{1}{2\pi(C_{nano} + C_{pad} + C_{stray} + C_{amp})R_{amp}} \quad (4.27)$
[69]	absent (4.28)
[70]	$\frac{1}{2\pi(C'_{dl} + C_{lsh} + C_{ain})R_{ain}} \quad (4.29)$
f_{p2}	
[This work]	$\frac{1}{2\pi(R_{njseal} + R_{jseal} + R_{nano} + R_{stray})} \left(\frac{1}{C_{nano}} + \frac{1}{C_{amp} + C_{stray}} \right) \quad (4.30)$
[69]	$\frac{R_e + R_{seal}}{2\pi R_e R_{seal} (C_{hd} + C_e)} \quad (4.31)$
[70]	$\frac{1}{2\pi(R_{jseal} + R_s)} \left(\frac{1}{C'_{dl}} + \frac{1}{C_{ain} + C_{lsh}} \right) \quad (4.32)$
f_{p3}	
[This work]	$\frac{1}{2\pi(C_{njm} + C_{pad})R_{stray}} \quad (4.33)$
[69]	absent (4.34)
[70]	absent (4.35)

Table 4. Comparison of the in-band gain and pole expressions of this work (first line in each row of the table) vs those of [69] (second line) and [70] (third line) for extracellular-passive system transfer functions. For comparison purposes we assume $R_{njseal} \ll R_{jseal}$ and set the parameter in [69] as: $C_{hd} = (C_{njm} + C_{jm})$, $C_e = C_{nano}$, $C_{sh} = C_{stray}$, $R_{met} = R_{stray}$, $R_e = \infty$; and in [70] as: $C'_{dl} = C_{nano}$, $C''_{dl} = 0$, $C'_{jm} = (C_{njm} + C_{jm})$, $C_{ain} = C_{amp}$, $R_{ain} = R_{amp}$, $C_{lsh} = C_{stray}$, $R_s \approx 0$.

our expression for $G_{in-band}$ (Eq. (4.24)) accounts for C_{stray} and C_{amp} which are present in [70] (Eq. (4.26)) but not in [69] (Eq. (4.25)). Therefore, Eq. (4.24) predicts a lower gain value than Eq. (4.25). However, if we eliminate the effect of R_{nano} , R_{stray} , C_{stray} , C_{amp} , R_{amp} , then the same in-band gain of [69] is found, as confirmed by the overlay between the blue and red curves in Fig. 9.

(e) Estimation of the Signal-to-Noise Ratio

The SNR is here defined as the ratio of the peak-to-peak V_{out} signal amplitude to three times the noise rms value: $SNR = V_{out}[V_{pp}] / (3V_{n,out}[V_{rms}])$, as in [48]. The output noise, $V_{n,out}$, is computed with noise simulations of the circuits in Fig. 4 by integrating the noise spectrum from 0.1 Hz to 10 kHz. For this analysis, the readout gain has been chosen (by adjusting R_1 , R_2 , R_{feed} as reported in Tab. A2 in the Additional information) to achieve a peak-to-peak $V_{out}[V_{pp}] = 1$

V response to an AP, a reasonable value to match the dynamic input range of typical integrated Analog to Digital Converters (ADC) in nowadays CMOS technologies [71].

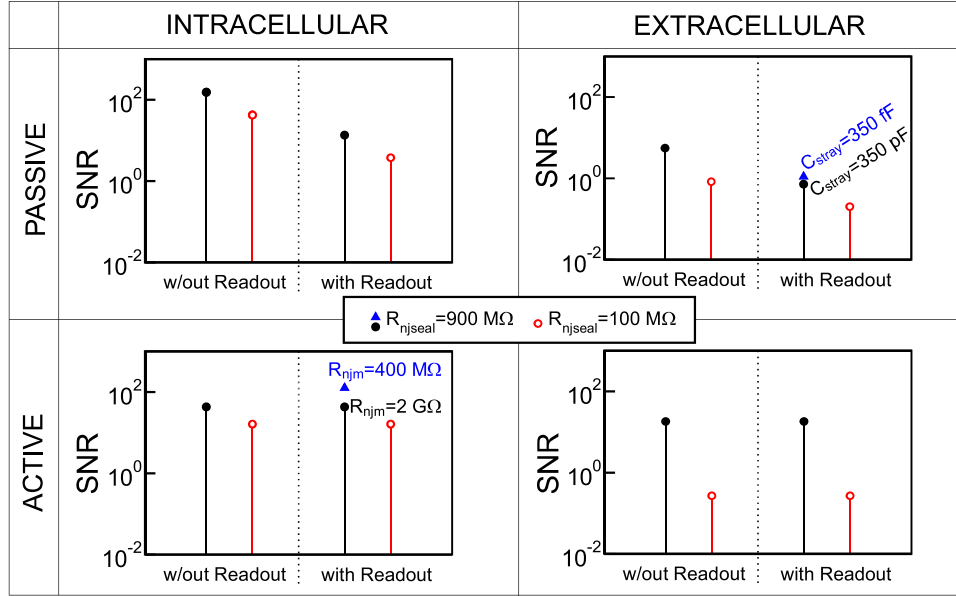


Figure 10. SNR evaluated as $V_{out}[V_{pp}]/3 \cdot V_{n,out}[V_{rms}]$ for the different sealing conditions, access types, and in presence or absence of readout noise. The readout gain has been set to provide recorded signals with 1 V_{pp} amplitudes by choosing the values of R_2 and R_{feed} as in Tab. A2.

The noise model accounts for the thermal noise of the resistive elements in Fig. 4, describing the semiconductor, the electrolyte, the interconnect parasitics, the external resistances in the readout amplifier, as well as the FET channel noise (equal to $4kTg_m$, where k is the Boltzmann constant and $T = 300K$ the temperature) [72], and the equivalent noise sources of a typical low noise OpAmp (e.g., $e_n = 7.5 \text{ nV/Hz}^{1/2}$, $i_n = 2 \text{ fA/Hz}^{1/2}$). The model neglects chemical [73] and biological noise, and the $1/f$ noise of the (MOS)FET, which are present in the real system where semiconductor devices are in contact with electrolytes [74]. Therefore, the computed SNR is a best case estimate, nevertheless still useful to compare the sensor/readout combinations.

Fig. 10 shows the SNR for different sealing conditions and access types. A first calculation (right portion of each graph) includes the readout noise, and provides more realistic estimate of the system SNR. The second one (left portion of each graph) provides a fair comparison between sensing devices alone, since the readout noise is excluded. Notice that R_{amp} is an equivalent input resistance and does not produce noise *per-sé*. The input referred noise of the readout, when included, is described by the equivalent noise sources of the OpAmp and the thermal noise of the amplifier circuit resistors. Fig. 10 shows that when the readout noise is turned off, the intracellular passive recording system yields the highest SNRs regardless of the sealing conditions. The lowest SNRs (even < 1 with the considered designs and parameter set) are found for the extracellular passive sensor. A smaller than 1 SNR is useless and should be avoided. If we reduce C_{stray} by three orders of magnitude (from 350 pF to 350 fF, top right plot in Fig. 10), the SNR of the passive-extracellular increases from ≈ 0.71 to a mere ≈ 1.11 , because the input capacitance of the OpAmp, $C_{amp} = 10 \text{ pF}$, is essentially in parallel to C_{stray} . We can then conclude that the choice of the readout and the optimization of the interconnects are critical in passive recording systems. An active pixel integrating the electrode with a low input capacitance readout next to it would certainly yield benefits.

For active sensing solutions the SNR is essentially unaffected by the readout noise (compare left and right halves of each graph in the bottom row), which has an impact, instead, on passive sensors. Poor sealing conditions degrade the SNR in all cases, and make it even smaller than one for extracellular sensors. If the readout noise is negligible, the SNR of intracellular active sensors is smaller than for the passive sensor. This may be due to the large bandwidth that, if not limited, captures a large integrated noise.

We further investigated ways to improve the performance of active FET sensors with *intracellular* coupling (a promising combination, insensitive to the readout noise in our test cases). We found that when R_{njseal} increases from 900 M Ω to 100 G Ω the SNR remains essentially constant and, furthermore, insensitive to large variations of C_{stray} . SNR improvements are obtained only when the R_{njm} decreases from the 2 G Ω value assumed in all calculations to 400 M Ω [39]. This suggests that R_{njm} is a major noise source for the intracellular active system, and that either an intimate contact to the cytosol, or a way to locally increase the membrane conductance, should be implemented [39] compared to the typical electroporation conditions (i.e., $R_{njm} \approx 2$ G Ω as mentioned in Section 3).

5. Conclusions

Micro-/nano-electrode arrays can interrogate neural signals ranging from short-term intracellular access to long-term extracellular recording, with all the shades in between. In perspective, they provide neuroscientists with a vast portfolio of advanced and scalable recording technologies. In this context, we have overviewed a few recent *in-vitro* neuron activity sensor devices, with an eye on semiconductor technology and integrated biochips, and with the perspective of enabling the study of the transduction process from the neuron to the readout for different sensor device's shape, materials, readouts,.

To gain insight on how the neuronal signals propagate to the sensor output, a multiscale-multiphysics modelling methodology based on TCAD tools has been developed and implemented, employing mixed-mode numerical FEM and circuit descriptions suited to limit the computational burden. The model is amenable to incorporate in the same simulation framework the solid-state devices (sensors and readout amplifier), the biological entities and their environment (neurons and sample electrolyte). The TCAD has been used to validate the compartmental circuit models and to explore a few sensor designs featuring different geometry and materials.

An extensive set of closed-form expressions for the transfer function between the intracellular potential and the output of the readout have been reported for both intra- and extracellular recording. They provide new insights about the influence of the main circuit elements on the recorded signal. In particular, the analysis points out that, consistently with the literature overview, intracellular recording yields larger monophasic signals, which faithfully retain the shape of the AP, while in the extracellular case the response can remarkably depart from the expected time derivative of the AP depending on the coupling between the neuron and the electrode or the distribution of ion channels along the cleft. The transfer functions provide useful insights on which part of the system affects the response. However, although the key predictions are consistent with the results in the time-domain analysis, the use of TFs is not accurate in predicting the sensed waveform for extracellular recording, due to the distributed nature of the membrane currents (see Section (c) in the Additional information).

The model was also used to estimate the thermal noise limited SNR and its dependence on the main features of the sensing system. The large signals offered by intracellular recording are partly spoiled by a wide equivalent noise bandwidth. Active recording makes the system insensitive to the readout amplifier noise, but more subject to $1/f$ noise components from the FET, not included yet in our analysis but increasingly important for nanoscale CMOS transistors. The detrimental role of poor sealing and high intracellular contact resistance conditions has been highlighted.

The developed methodology and its implementation are well suited to investigate the impact of various technology options, and it can support device engineering and optimization

as also exemplified in this work. Furthermore, the model is amenable to extensions aimed at incorporating more complex physical effects and noise sources, more realistic neuron morphology, as derived for instance by real culture imaging, better discretizations of its compartments, possibly derived by extensive physical characterizations, and last but not least cross-talk effects among adjacent sensors.

Data Accessibility. The additional information supporting this article have been uploaded as part of the supplementary material. Input decks for simulations and datasets have been uploaded on Zenodo doi: 10.5281/zenodo.5562681 [76]

Authors' Contributions. FL carried out the model implementation and the simulations. All authors contributed equally to conceiving the design of the study, analysing the data, drafting the manuscript. All authors read and approved the manuscript.

Competing Interests. The author(s) declare that they have no competing interests.

Funding. This work has been financially supported by the European Union's Horizon-2020 project "IN-FET" (Grant Agreement n. 862882).

Acknowledgements. The authors acknowledge useful technical discussions with all the partners of the H2020 EC project "IN-FET".

References

- Widdershoven F, Cossetti A, Laborde C, Bandiziol A, van Swinderen PP, Lemay SG, et al. 2018. A CMOS Pixelated Nanocapacitor Biosensor Platform for High-Frequency Impedance Spectroscopy and Imaging. *IEEE Trans Biomed Circuits Syst* **12**, 1369–82. (<http://dx.doi.org/10.1109/TBCAS.2018.2861558>)
- Jiang Y, Tian B. 2018. Inorganic semiconductor biointerfaces. *Nat Rev Mater* **3**, 473–90. (<http://dx.doi.org/10.1038/s41578-018-0062-3>)
- Zhou W, Dai X, Lieber CM. 2016. Advances in nanowire bioelectronics. *Rep Prog Phys* **80**, 016701. (<http://dx.doi.org/10.1088/0034-4885/80/1/016701>)
- Zhang A, Lee J-H, Lieber CM. 2021. Nanowire-enabled bioelectronics. *Nano Today* **38**, 101135. (<http://dx.doi.org/10.1016/j.nantod.2021.101135>)
- Berdondini L, Imfeld K, Maccione A, Tedesco M, Neukom S, Koudelka-Hep M, et al. 2009. Active pixel sensor array for high spatio-temporal resolution electrophysiological recordings from single cell to large scale neuronal networks. *Lab Chip* **29**, 2644. (<http://dx.doi.org/10.1039/B907394A>).
- Abbott J, Ye T, Park H, Ham D. 2019. CMOS interface with biological molecules and cells. *IEEE 45th European Solid State Circuits Conference (ESSCIRC)* (<http://dx.doi.org/10.1109/ESSCIRC.2019.8902832>)
- Hierlemann A, Frey U, Hafizovic S, Heer F. 2011. Growing Cells Atop Microelectronic Chips: Interfacing Electrogenic Cells In Vitro With CMOS-Based Microelectrode Arrays. *Proc IEEE* **99**, 252–84. (<http://dx.doi.org/10.1109/JPROC.2010.2066532>)
- Wu Y, Chen H, Guo L. 2020. Opportunities and dilemmas of in vitro nano neural electrodes. *RSC* **10**, 187–200. (<http://dx.doi.org/10.1039/c9ra08917a>)
- Tian B, Lieber CM. 2019. Nanowired Bioelectric Interfaces. *Chem Rev* **119**, 9136–52. (<http://dx.doi.org/10.1021/acs.chemrev.8b00795>)
- Choi JS, Lee HJ, Rajaraman S, Kim D-H. 2021. Recent advances in three-dimensional microelectrode array technologies for in vitro and in vivo cardiac and neuronal interfaces. *Biosensors and Bioelectronics* **171**, 112687. (<http://dx.doi.org/10.1016/j.bios.2020.112687>)
- Robinson JT, Xie C, Pohlmeyer E, Gather MC, Kemere C, Kitching JE, et al. 2019. Developing Next-Generation Brain Sensing Technologies—A Review. *IEEE Sensors J* **19**, 10163–75. (<http://dx.doi.org/10.1109/JSEN.2019.2931159>)
- Maiolo L, Polese D, Convertino A. 2019. The rise of flexible electronics in neuroscience, from materials selection to in vitro and in vivo applications. *Advances in Physics: X* **4**, 1664319. (<http://dx.doi.org/10.1080/23746149.2019.1664319>)
- Soscia DA, Lam D, Tooker AC, Enright HA, Triplett M, Karande P, et al. 2020. A flexible 3-dimensional microelectrode array for in vitro brain models. *Lab Chip* **20**, 901–11.

- (<http://dx.doi.org/10.1039/C9LC01148J>)
14. Yi N, Cui H, Zhang LG, Cheng H. 2019. Integration of biological systems with electronic-mechanical assemblies. *Acta Biomaterialia* **95**, 91–111. (<http://dx.doi.org/10.1016/j.actbio.2019.04.032>)
 15. Vassanelli S, Mahmud M. 2016. Trends and Challenges in Neuroengineering: Toward “Intelligent” Neuroprostheses through Brain–“Brain Inspired Systems” Communication. *Front Neurosci* **10**. (<http://dx.doi.org/10.3389/fnins.2016.00438>)
 16. Chiappalone M, Pasquale V, Frega M, editors. 2019. *In Vitro Neuronal Networks. Advances in Neurobiology*. CH:Springer International Publishing. <http://dx.doi.org/10.1007/978-3-030-11135-9>
 17. Massobrio P, Massobrio G, Martinoia S. 2016. Interfacing Cultured Neurons to Microtransducers Arrays: A Review of the Neuro-Electronic Junction Models. *Front Neurosci* **21**, 10. (<http://dx.doi.org/10.3389/fnins.2016.00282>)
 18. Massobrio G, Martinoia S, Massobrio P. 2018. Equivalent Circuit of the Neuro-Electronic Junction for Signal Recordings From Planar and Engulfed Micro-Nano-Electrodes. *IEEE Trans Biomed Circuits Syst* **12**, 3–12. (<http://dx.doi.org/10.1109/TBCAS.2017.2749451>)
 19. Guo L. 2019. On neural recording using nanoprotrusion electrodes. *J Neural Eng* **17**, 016017. (<http://dx.doi.org/10.1088/1741-2552/ab51de>)
 20. Abbott J, Ye T, Qin L, Jorgolli M, Gertner RS, Ham D, et al. 2017. CMOS nanoelectrode array for all-electrical intracellular electrophysiological imaging. *Nature Nanotech* **12**, 460–6. (<http://dx.doi.org/10.1038/nnano.2017.3>)
 21. Hanson L, Lin ZC, Xie C, Cui Y, Cui B. 2012. Characterization of the Cell–Nanopillar Interface by Transmission Electron Microscopy. *Nano Lett* **12**, 5815–20. (<http://dx.doi.org/10.1021/nl303163y>)
 22. Santoro F, Zhao W, Joubert L-M, Duan L, Schnitker J, van de Burgt Y, et al. 2017. Revealing the Cell–Material Interface with Nanometer Resolution by Focused Ion Beam/Scanning Electron Microscopy. *ACS Nano* **11**, 8320–8. (<http://dx.doi.org/10.1021/acsnano.7b03494>)
 23. Marani E, Rutten WLC, Buitengeweg JR. 2000. Finite element modeling of the neuron-electrode interface. *IEEE Eng Med Biol Mag* **19**, 46–52. (<http://dx.doi.org/10.1109/51.887245>)
 24. Thomasjr C, Springer P, Loeb G, Berwaldnetter Y, Okun L. 1972. A miniature microelectrode array to monitor the bioelectric activity of cultured cells. *Experimental Cell Research* **74**, 61–6. ([http://dx.doi.org/10.1016/0014-4827\(72\)90481-8](http://dx.doi.org/10.1016/0014-4827(72)90481-8))
 25. Pine J. 1980. Recording action potentials from cultured neurons with extracellular microcircuit electrodes. *Journal of Neuroscience Methods* **2**, 19–31. ([http://dx.doi.org/10.1016/0165-0270\(80\)90042-4](http://dx.doi.org/10.1016/0165-0270(80)90042-4))
 26. Joye N, Schmid A, Leblebici Y. 2009. Electrical modeling of the cell–electrode interface for recording neural activity from high-density microelectrode arrays. *Neurocomputing* **73**, 250–9. (<http://dx.doi.org/10.1016/j.neucom.2009.09.006>)
 27. Spira ME, Hai A. 2013. Multi-electrode array technologies for neuroscience and cardiology. *Nature Nanotech* **8**, 83–94. (<http://dx.doi.org/10.1038/nnano.2012.265>)
 28. Fromherz P, Offenhausser A, Vetter T, Weis J. 1991. A neuron-silicon junction: a Retzius cell of the leech on an insulated-gate field-effect transistor. *Science* **252**, 1290–3. (<http://dx.doi.org/10.1126/science.1925540>)
 29. Schätzthauer R, Fromherz P. 1998. Neuron-silicon junction with voltage-gated ionic currents. *European Journal of Neuroscience* **10**, 1956–62. (<http://dx.doi.org/10.1046/j.1460-9568.1998.00205.x>)
 30. Zeck G, Fromherz P. 2001. Noninvasive neuroelectronic interfacing with synaptically connected snail neurons immobilized on a semiconductor chip. *Proceedings of the National Academy of Sciences* **98**, 10457–62. (<http://dx.doi.org/10.1073/pnas.181348698>)
 31. Patolsky F. Detection, Stimulation, and Inhibition of Neuronal Signals with High-Density Nanowire Transistor Arrays. 2006. *Science* **313**, 1100–4. (<http://dx.doi.org/10.1126/science.1128640>)
 32. <https://www.multichannelsystems.com/>
 33. Tsai D, Sawyer D, Bradd A, Yuste R, Shepard KL. 2017. A very large-scale microelectrode array for cellular-resolution electrophysiology. *Nat Commun* **8**. (<http://dx.doi.org/10.1038/s41467-017-02009-x>)
 34. Fu T-M, Duan X, Jiang Z, Dai X, Xie P, Cheng Z, et al. 2014. Sub-10-nm intracellular bioelectronic probes from nanowire-nanotube heterostructures. *Proceedings of the National Academy of Sciences* **111**, 1259–64. (<http://dx.doi.org/10.1073/pnas.1323389111>)

35. Ojovan SM, Rabieh N, Shmoel N, Erez H, Maydan E, Cohen A, et al. 2015. A feasibility study of multi-site, intracellular recordings from mammalian neurons by extracellular gold mushroom-shaped microelectrodes. *Sci Rep* **5**. (<http://dx.doi.org/10.1038/srep14100>)
36. Spira ME, Shmoel N, Huang S-HM, Erez H. 2018. Multisite Attenuated Intracellular Recordings by Extracellular Multielectrode Arrays, a Perspective. *Front Neurosci* **12**. (<http://dx.doi.org/10.3389/fnins.2018.00212>)
37. Jones PD, Moskalyuk A, Barthold C, Gutöhrlein K, Heusel G, Schröppel B, et al. 2020. Low-Impedance 3D PEDOT:PSS Ultramicroelectrodes. *Front Neurosci* **14**. (<http://dx.doi.org/10.3389/fnins.2020.00405>)
38. Dipalo M, Amin H, Lovato L, Moia F, Caprettini V, Messina GC, et al. 2017. Intracellular and Extracellular Recording of Spontaneous Action Potentials in Mammalian Neurons and Cardiac Cells with 3D Plasmonic Nanoelectrodes. *Nano Lett* **17**, 3932–9. (<http://dx.doi.org/10.1021/acs.nanolett.7b01523>)
39. Abbott J, Ye T, Krensek K, Gertner RS, Ban S, Kim Y, et al. 2019. A nanoelectrode array for obtaining intracellular recordings from thousands of connected neurons. *Nat Biomed Eng* **4**, 232–41. (<http://dx.doi.org/10.1038/s41551-019-0455-7>)
40. Rivnay J, Leleux P, Ferro M, Sessolo M, Williamson A, Koutsouras DA, et al. 2015. High-performance transistors for bioelectronics through tuning of channel thickness. *Sci Adv* **1**, e1400251. (<http://dx.doi.org/10.1126/sciadv.1400251>)
41. Martin DC, Malliaras GG. 2016. Interfacing Electronic and Ionic Charge Transport in Bioelectronics. *ChemElectroChem* **3**, 686–8. (<http://dx.doi.org/10.1002/celec.201500555>)
42. Abbott J, Ye T, Krensek K, Gertner RS, Wu W, Jung HS, et al. 2020. Extracellular recording of direct synaptic signals with a CMOS-nanoelectrode array. *Lab Chip* **20**, 3239–48. (<http://dx.doi.org/10.1039/d0lc00553c>)
43. He G, Hu N, Xu AM, Li X, Zhao Y, Xie X. 2020. Nanoneedle Platforms: The Many Ways to Pierce the Cell Membrane. *Adv Funct Mater* **30**, 1909890. (<http://dx.doi.org/10.1002/adfm.201909890>)
44. Liu R, Chen R, Elthakeb AT, Lee SH, Hinckley S, Khraiche ML, et al. 2017. High Density Individually Addressable Nanowire Arrays Record Intracellular Activity from Primary Rodent and Human Stem Cell Derived Neurons. *Nano Lett* **17**, 2757–64. (<http://dx.doi.org/10.1021/acs.nanolett.6b04752>)
45. Lee J-H, Zhang A, You SS, Lieber CM. 2016. Spontaneous Internalization of Cell Penetrating Peptide-Modified Nanowires into Primary Neurons. *Nano Lett* **16**, 1509–13. (<http://dx.doi.org/10.1021/acs.nanolett.6b00020>)
46. Hai A, Spira ME. 2012. On-chip electroporation, membrane repair dynamics and transient in-cell recordings by arrays of gold mushroom-shaped microelectrodes. *Lab Chip* **12**, 2865. (<http://dx.doi.org/10.1039/c2lc40091j>)
47. Almquist BD, Melosh NA. 2010. Fusion of biomimetic stealth probes into lipid bilayer cores. *Proceedings of the National Academy of Sciences* **107**, 5815–20. (<http://dx.doi.org/10.1073/pnas.0909250107>)
48. Zhao Y, You SS, Zhang A, Lee J-H, Huang J, Lieber CM. 2019. Scalable ultrasmall three-dimensional nanowire transistor probes for intracellular recording. *Nat Nanotechnol* **14**, 783–90. (<https://doi.org/10.1038/s41565-019-0478-y>)
49. Tian B, Cohen-Karni T, Qing Q, Duan X, Xie P, Lieber CM. 2010. Three-Dimensional, Flexible Nanoscale Field-Effect Transistors as Localized Bioprobes. *Science* **329**, 830–4. (<http://dx.doi.org/10.1126/science.1192033>)
50. Gao R, Strehle S, Tian B, Cohen-Karni T, Xie P, Duan X, et al. 2012. Outside Looking In: Nanotube Transistor Intracellular Sensors. *Nano Lett* **12**, 3329–33. (<http://dx.doi.org/10.1021/nl301623p>)
51. Duan X, Gao R, Xie P, Cohen-Karni T, Qing Q, Choe HS, et al. 2011. Intracellular recordings of action potentials by an extracellular nanoscale field-effect transistor. *Nature Nanotech* **7**, 174–9. (<http://dx.doi.org/10.1038/NNANO.2011.223>)
52. Storm JF. 1987. Action potential repolarization and a fast after-hyperpolarization in rat hippocampal pyramidal cells. *The Journal of Physiology* **385**, 733–59. (<http://dx.doi.org/10.1113/jphysiol.1987.sp016517>)
53. Synopsys website: <https://www.synopsys.com/silicon/tcad.html>.
54. Chung I-Y, Jang H, Lee J, Moon H, Seo SM, Kim DH. 2012. Simulation study on discrete charge effects of SiNW biosensors according to bound target position using a 3D TCAD simulator. *Nanotechnology* **23**, 065202. (<http://dx.doi.org/10.1088/0957-4484/23/6/065202>)

55. Pittino F, Palestri P, Scarbolo P, Esseni D, Selmi L. 2014. Models for the use of commercial TCAD in the analysis of silicon-based integrated biosensors. *Solid-State Electronics* **98**, 63–9. (<http://dx.doi.org/10.1016/j.sse.2014.04.011>)
56. Bandiziol A, Palestri P, Pittino F, Esseni D, Selmi L. 2015. A TCAD-Based Methodology to Model the Site-Binding Charge at ISFET/Electrolyte Interfaces. *IEEE Trans Electron Devices* **62**, 3379–86. (<http://dx.doi.org/10.1109/TED.2015.2464251>)
57. Synopsys. 2015. *Sentaurus Device User Guide*, US: Mountain View, CA.
58. Leva F, Palestri P, Selmi L. 2021. Modelling of vertical nano-needles as sensing devices for neuronal signal recordings. *IEEE preprint*. (<http://dx.doi.org/10.36227/techrxiv.12585086.v2>)
59. Harris JJ, Jolivet R, Engl E, Attwell D. 2015. Energy-Efficient Information Transfer by Visual Pathway Synapses. *Current Biology* **25**, 3151–60. (<http://dx.doi.org/10.1016/j.cub.2015.10.063>)
60. Martinoia S, Massobrio P, Bove M, Massobrio G. 2004. Cultured Neurons Coupled to Microelectrode Arrays: Circuit Models, Simulations and Experimental Data. *IEEE Trans Biomed Eng* **51**, 859–64. (<http://dx.doi.org/10.1109/TBME.2004.826607>)
61. Hodgkin AL, Huxley AF. 1952. A quantitative description of membrane current and its application to conduction and excitation in nerve. *The Journal of Physiology* **117**, 500–44. (<http://dx.doi.org/10.1113/jphysiol.1952.sp004764>)
62. Chua L. 1980. Device modeling via nonlinear circuit elements. *IEEE Trans Circuits Syst* **27**, 1014–44. (<http://dx.doi.org/10.1109/TCS.1980.1084742>)
63. Parodi M, Storace M. 1997. On a circuit representation of the Hodgkin and Huxley nerve axon membrane equations. *Int J Circ Theor Appl* **25**, 115–124. ([http://dx.doi.org/10.1002/\(SICI\)1097-007X\(199703/04\)25:2<115::AID-CTA957>3.0.CO;2-#](http://dx.doi.org/10.1002/(SICI)1097-007X(199703/04)25:2<115::AID-CTA957>3.0.CO;2-#))
64. Bielek D, Biolkova V, Kolka Z. 2013. Spice models of memristive devices forming a model of Hodgkin-Huxley axon. *2013 18th International Conference on Digital Signal Processing (DSP) IEEE*. (<http://dx.doi.org/10.1109/ICDSP.2013.6622743>)
65. Silverthorn D U. 2018. *Human Physiology: An Integrated Approach*. Eighth edition. US: Pearson.
66. Robinson JT, Jorgolli M, Shalek AK, Yoon M-H, Gertner RS, Park H. 2012. Vertical nanowire electrode arrays as a scalable platform for intracellular interfacing to neuronal circuits. *Nature Nanotech* **7**, 180–4. (<http://dx.doi.org/10.1038/nnano.2011.249>)
67. Jaeger R C, Blalock T N. 2010. *Microelectronic circuit design*. Fourth edition. US: McGraw-Hill.
68. SCAM website: <https://lpsa.swarthmore.edu/Systems/Electrical/mna/MNA1.html>.
69. Massobrio P, Massobrio G, Martinoia S. 2007. Multi-program approach for simulating recorded extracellular signals generated by neurons coupled to microelectrode arrays. *Neurocomputing* **70**, 2467–76. (<http://dx.doi.org/10.1016/j.neucom.2006.09.008>)
70. Guo L. 2020. Perspectives on electrical neural recording: a revisit to the fundamental concepts. *J Neural Eng* **17**, 013001. (<http://dx.doi.org/10.1088/1741-2552/ab702f>)
71. Pagin M, Ortmanns M. 2017. Evaluation of logarithmic vs. linear ADCs for neural signal acquisition and reconstruction. *39th Annual International Conference of the IEEE Engineering in Medicine and Biology Society (EMBC)*. (<http://dx.doi.org/10.1109/EMBC.2017.8037828>)
72. Thomas H. Lee. 2004. *The Design of CMOS Radio-Frequency Integrated Circuits*. UK: Cambridge University Press.
73. Mele LJ, Palestri P, Selmi L. 2019. A model of the interface charge and chemical noise due to surface reactions in Ion Sensitive FETs. *International Conference on Simulation of Semiconductor Processes and Devices (SISPAD) IEEE*. (<http://dx.doi.org/10.1109/SISPAD.2019.8870563>)
74. Bellando F, Mele LJ, Palestri P, Zhang J, Ionescu AM, Selmi L. 2021. Sensitivity, Noise and Resolution in a BEOL-Modified Foundry-Made ISFET with Miniaturized Reference Electrode for Wearable Point-of-Care Applications. *Sensors* **21**, 1779. (<http://dx.doi.org/10.3390/s21051779>)
75. Barboni L. 2020. Evidence of Limitations of the Transconductance-to-Drain-Current Method (gm/Id) for Transistor Sizing in 28 nm UTBB FD-SOI Transistors. *JLPEA* **10**, 17. (<http://dx.doi.org/10.3390/jlpea10020017>)
76. Zenodo repository: <https://doi.org/10.5281/zenodo.5562681>.